

UCLA

UCLA Previously Published Works

Title

Spatial regulation of AMPK signaling revealed by a sensitive kinase activity reporter

Permalink

<https://escholarship.org/uc/item/40w6s5tn>

Journal

Nature Communications, 13(1)

ISSN

2041-1723

Authors

Schmitt, Danielle L
Curtis, Stephanie D
Lyons, Anne C
[et al.](#)

Publication Date





2022

DOI

10.1038/s41467-022-31190-x

Peer reviewed

Spatial regulation of AMPK signaling revealed by a sensitive kinase activity reporter

Danielle L. Schmitt¹, Stephanie D. Curtis², Anne C. Lyons³, Jin-fan Zhang³, Mingyuan Chen ³, Catherine Y. He¹, Sohum Mehta ¹, Reuben J. Shaw ² & Jin Zhang ^{1,3,4}✉

AMP-activated protein kinase (AMPK) is a master regulator of cellular energetics which coordinates metabolism by phosphorylating a plethora of substrates throughout the cell. But how AMPK activity is regulated at different subcellular locations for precise spatiotemporal control over metabolism is unclear. Here we present a sensitive, single-fluorophore AMPK activity reporter (ExRai AMPKAR), which reveals distinct kinetic profiles of AMPK activity at the mitochondria, lysosome, and cytoplasm. Genetic deletion of the canonical upstream kinase liver kinase B1 (LKB1) results in slower AMPK activity at lysosomes but does not affect the response amplitude at lysosomes or mitochondria, in sharp contrast to the necessity of LKB1 for maximal cytoplasmic AMPK activity. We further identify a mechanism for AMPK activity in the nucleus, which results from cytoplasmic to nuclear shuttling of AMPK. Thus, ExRai AMPKAR enables illumination of the complex subcellular regulation of AMPK signaling.

¹Department of Pharmacology, University of California San Diego, La Jolla, CA, USA. ²Molecular and Cell Biology Laboratory, The Salk Institute for Biological Studies, La Jolla, CA, USA. ³Department of Bioengineering, University of California San Diego, La Jolla, CA, USA. ⁴Department of Chemistry and Biochemistry, University of California San Diego, La Jolla, CA, USA. ✉email: jzhang32@ucsd.edu

AMP-activated protein kinase (AMPK) is a ubiquitously expressed heterotrimeric protein in mammals, composed of one of two α kinase subunits, one of two β regulatory subunits, and one of three γ nucleotide-binding subunits¹. Allosteric activation of AMPK is achieved through binding of adenine nucleotides to the γ subunit or small molecules to the allosteric drug and metabolite (ADAM) site at the interface between α and β subunits^{2,3}. AMPK is regulated by several upstream kinases, predominantly liver kinase B1 (LKB1)^{4,5} and calcium/calmodulin protein kinase kinase 2 (CaMKK2)⁶, to control metabolic processes including glycolysis, lipid and protein biosynthesis, mitochondrial biogenesis, and gene expression^{7,8}.

How AMPK senses different stimuli and relays diverse signals to downstream components in various subcellular locations with high specificity has remained elusive. An emerging view is that compartmentalized AMPK signaling enables specificity toward downstream effectors^{9,10}. Signaling complexes containing AMPK are found at different subcellular locations, including lysosomes, mitochondria, endoplasmic reticulum, and the nucleus⁷. Recent studies found that lysosomal pools of AMPK are preferentially activated by glucose starvation, whereas more severe metabolic stressors like glutamine starvation or pharmacological stimulation are required to activate cytoplasmic and mitochondrial pools of AMPK, due to specific assembly of lysosomal AMPK-activating signaling complexes¹¹. However, our understanding of the regulation of AMPK signaling at different subcellular locations is still limited, and AMPK regulation in specific locations remains controversial^{9,10}.

Genetically encoded reporters are powerful tools for interrogating the precise spatiotemporal regulation of signaling pathways^{12,13}. Addition of localization tags for cellular organelles and compartments to kinase activity reporters enables subcellular resolution of kinase activities in single cells, allowing for the elucidation of compartment-specific signaling mechanisms^{14,15}. This approach enabled us to profile subcellular AMPK activity using a Förster Resonance Energy Transfer (FRET)-based AMPK activity reporter¹⁶. However, the dynamic range of the current FRET-based AMPK activity reporters limited our ability to fully distinguish the dynamics and regulation of spatiotemporal AMPK activity^{15–19}.

In this work, we develop a single-fluorophore excitation-ratiometric AMPK activity reporter (ExRai AMPKAR), which reports endogenous AMPK activity in living cells with high sensitivity. Using our reporter, we profile spatiotemporal AMPK activity and find spatially defined roles for LKB1 in regulating cytoplasmic, lysosomal, and mitochondrial AMPK activity. Finally, we measure nuclear AMPK activity with ExRai AMPKAR and identify a regulatory mechanism for nuclear AMPK activity in living cells. This work provides a better understanding of spatiotemporal AMPK activity, which is critical for the diverse signaling profile of AMPK throughout the cell.

Results

Development of an excitation-ratiometric AMPK activity reporter. Building on our recent success in engineering single-fluorophore-based kinase activity reporters with high dynamic range^{20,21}, we set out to develop a single-fluorophore AMPKAR. The modular design of biosensors enables coupling of different activity sensing units with readout-generating reporting units to create new biosensors^{22,23}. We inserted a circularly permuted enhanced green fluorescent protein (cpEGFP), a widely used reporting unit²⁴, between the two components of the AMPK activity sensing unit from a previous FRET-based AMPK biosensor¹⁸, which consists of an AMPK substrate domain¹⁷ and the phosphoamino acid-binding forkhead associated domain 1

(FHA1). Upon phosphorylation of the reporter and binding of the FHA1 domain to the phosphorylated AMPK substrate sequence, we expect to observe an increase in fluorescence emission with 480 nm excitation and a decrease with 400 nm excitation (Fig. 1a). The ratio of these two fluorescence intensities (Ex 480 nm/400 nm) can be used as an excitation ratiometric readout (R). Given that linkers at the junctions of the sensing unit and reporting unit are particularly important in determining the dynamic range of the reporter²⁵, we set out to vary the two amino acids immediately flanking either side of cpEGFP to identify a linker combination that would result in a large excitation ratio change upon AMPK stimulation. The top five linkers from our previous screen to generate a high-performance excitation-ratiometric protein kinase A activity reporter were selected²¹, and we tested the linker variants in Cos7 cells stimulated with an AMPK activator, 2-deoxyglucose (2-DG, Supplementary Fig. 1a). From this linker screen, we found the linker combination FC/LL yielded the largest maximum ratio change ($\Delta R/R_0$), and this variant was selected for further characterization.

Stimulation of AMPK using 2-DG in Cos7 cells expressing this reporter led to a large change in the excitation ratio ($\Delta R/R_0 = 1.80 \pm 0.29$; Fig. 1b, c and Supplementary Fig. 1b), whereas mutating the phosphorylation site threonine to alanine (T/A) to generate a phospho-null mutant resulted in a biosensor with minimal response ($\Delta R/R_0 = 0.075 \pm 0.0064$, $p < 0.0001$). We tested the reversibility of the response using the AMPK inhibitor SBI-0206965 (SBI)^{26,27}. In HEK293T cells expressing the reporter construct, 2-DG-stimulated AMPK activity was rapidly suppressed by SBI-0206965 to near basal levels ($R = 1.11 \pm 0.011$; Fig. 1d). Similarly, pretreatment with SBI-0206965 blocked the 2-DG-induced reporter response ($\Delta R/R_0 = 0.17 \pm 0.011$). We confirmed the ratio changes of ExRai AMPKAR are well correlated with phosphorylation of endogenous AMPK substrates (Supplementary Fig. 1c–e). To confirm the reporter responses are specific for AMPK activity, we expressed our biosensor in either wild-type or AMPK α 1/2 knockout mouse embryonic fibroblasts (WT or AMPK α KO MEFs, Supplementary Fig. 1f)²⁸. Treatment with SBI led to a decrease in the excitation ratio in WT MEFs, but not AMPK α KO MEFs (Supplementary Fig. 1g), suggesting presence of basal AMPK activity in WT MEFs. 2-DG stimulation induced large excitation-ratio increases in WT MEFs, whereas minimal responses were observed in AMPK α KO MEFs (Fig. 1e and Supplementary Fig. 1d), further demonstrating the specificity of the biosensor response. We observed a large variability in reporter response, and comparison of initial fluorescence (ex 400 nm) to $\Delta R/R_0$ did not show a strong correlation (Supplementary Fig. 1h). Previous studies have shown heterogeneous AMPK activity in a cell population when assessed at a single-cell level²⁹, which is likely observed here with our biosensor.

Finally, we compared our new construct to our previous FRET-based reporter¹⁸. In HEK293T cells stimulated with 2-DG, the excitation-ratio change from our new construct ($\Delta R/R_0 = 1.40 \pm 0.072$) was larger than the yellow/cyan emission ratio change from the FRET-based biosensor ($\Delta R/R_0 = 0.39 \pm 0.024$, $p < 0.0001$; Fig. 1f), which translated to a higher signal-to-noise ratio (SNR; FRET biosensor: 59.11 ± 6.46 vs. new construct: 228.1 ± 12.81 , $p < 0.0001$, Supplementary Fig. 1i). We also estimated the Z-factor, a measurement of assay fitness³⁰. From the average responses of these two reporters, the FRET-based biosensor had a Z-factor of 0.44, while our new construct had a Z-factor of 0.90, indicating better assay fitness. Thus, we have developed an AMPK activity reporter which we termed excitation-ratiometric AMPKAR (ExRai AMPKAR), for specific monitoring of dynamic AMPK activity within living cells with greatly enhanced sensitivity.

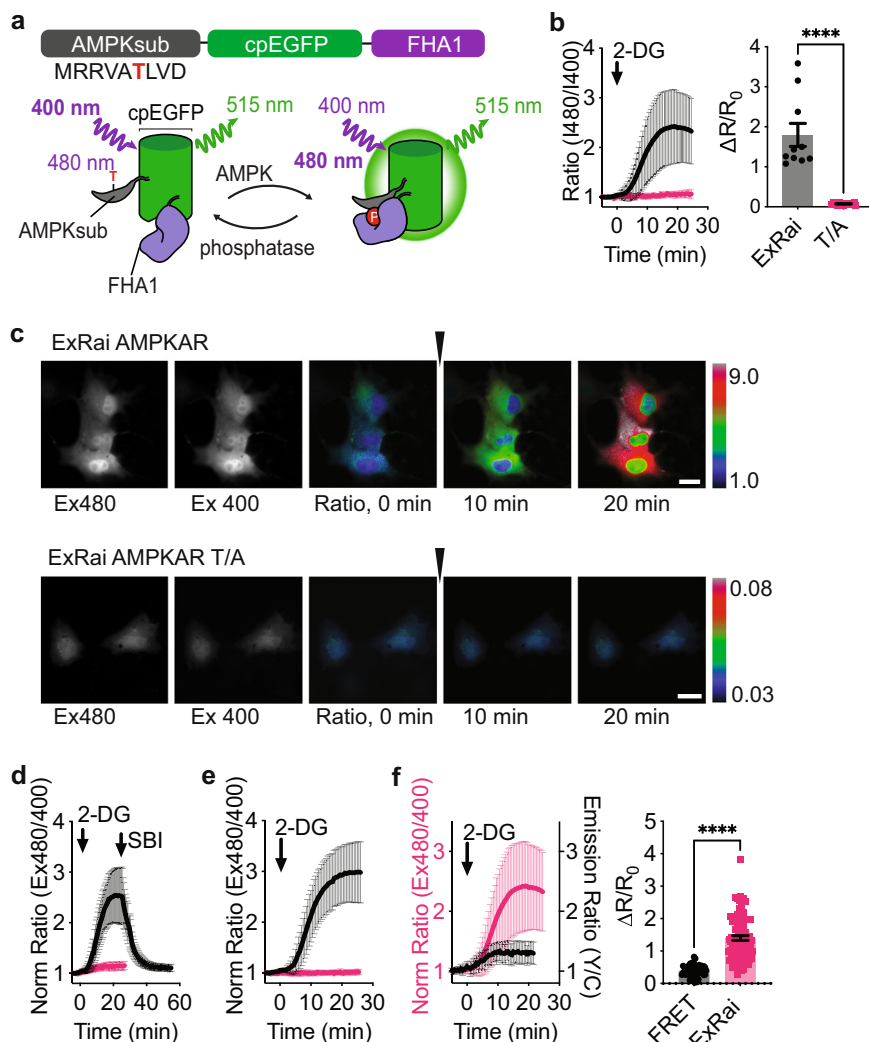


Fig. 1 Development and characterization of ExRai AMPKAR. **a** Design and domain structure of ExRai AMPKAR. Threonine phosphorylated by AMPK denoted in red. **b** Average response of ExRai AMPKAR (black, $n = 10$ cells from three experiments), and ExRai AMPKAR T/A (pink, $n = 17$ cells from three experiments) to 2-DG (40 mM) stimulation in Cos7 cells along with maximum ratio change (**** $p = 3.05 \times 10^{-8}$, unpaired t -test, two-tailed). **c** Representative images of ExRai AMPKAR (top) and ExRai AMPKAR T/A (bottom) in Cos7 cells treated with 2-DG (40 mM) at the indicated time. **d** Average response of ExRai AMPKAR to AMPK stimulation by 2-DG (40 mM) followed by SBI-0206965 (SBI, 30 μ M, black, $n = 35$ cells from three experiments) or after pretreatment with SBI-0206965 in HEK293T cells (pink, $n = 43$ cells from four experiments). **e** Average response of ExRai AMPKAR in WT MEFs (black, $n = 31$ cells from four experiments) and AMPK α KO MEFs (pink, $n = 23$ cells from four experiments) treated with 2-DG (40 mM). **f** Response of ExRai AMPKAR (pink, $n = 90$ cells from five experiments) and FRET-based AMPK reporter ABKAR (black trace, $n = 25$ cells from two experiments) in HEK293T cells treated with 2-DG (40 mM), along with maximum ratio change (**** $p = 4.31 \times 10^{-19}$, unpaired t -test, two-tailed). For all figures, time courses show the mean \pm SD, dot plots show the mean \pm SEM. Scale bars, 20 μ m.

Differential regulation of AMPK activity at the mitochondria and lysosome.

The mitochondria and lysosome represent key signaling locations for AMPK^{11,28,31–35}. Notably, results from western blotting assays have indicated that lysosomal pools of AMPK are preferentially activated under glucose deprivation, due to a lysosomal-localized AMPK regulatory complex³⁶, while mitochondrial AMPK is activated under more severe nutrient stress¹¹. However, dynamic AMPK activities have not been systematically analyzed at these two locations. Therefore, we deployed ExRai AMPKAR to better understand the spatio-temporal dynamics of AMPK at the lysosome and mitochondria. To specifically investigate lysosomal and mitochondrial AMPK activity, we fused ExRai AMPKAR to lysosome-associated membrane protein 1 (LAMP1) or a mitochondria-targeting sequence from dual specific A-kinase anchoring protein 1 (DAKAP1), respectively (Fig. 2a). We expressed the targeted

reporters in either WT or AMPK α KO MEFs and confirmed targeted ExRai AMPKARs were well-localized to each respective compartment by performing fluorescence recovery after photobleaching (FRAP) on each reporter (Supplementary Fig. 2a). Comparison of basal starting intensity revealed ExRai AMPKAR localized to membranous organelles had a higher starting ratio than cytoplasmic ExRai AMPKAR, consistent with our previous findings¹⁶ (Supplementary Fig. 2b). WT and AMPK α KO MEFs expressing either lysosomal-targeted ExRai AMPKAR or mitochondrial-targeted ExRai AMPKAR were treated with multiple concentrations of 2-DG (Fig. 2b, c and Supplementary Fig. 2c). We compared the time-to-half-maximum ($t_{1/2}$) of localized ExRai AMPKAR responses to 2-DG to identify kinetic differences amongst these locations. Lysosomal activity increased more rapidly than either cytoplasmic or mitochondrial activity ($t_{1/2} = 3.09 \pm 0.30$ min, $p \leq 0.0033$; Fig. 2d).

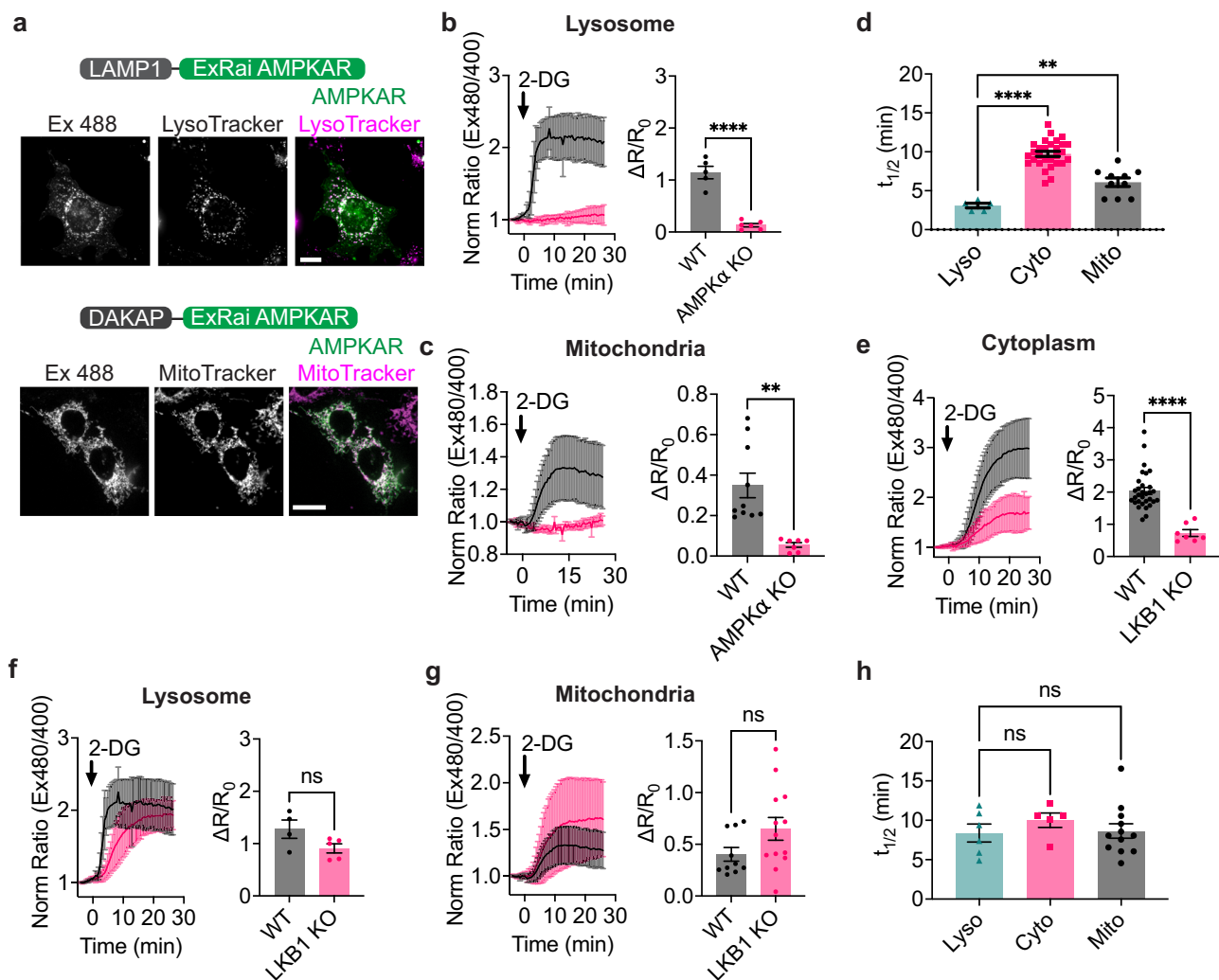


Fig. 2 Lysosomal AMPK activity is rapidly induced in an LKB1-dependent manner. **a** (Top) Domain layout and representative image of lyso-ExRai AMPKAR in MEFs stained with the lysosomal marker LysoTracker Red. (Bottom) Domain layout and representative image of mito-ExRai AMPKAR in MEFs stained with the mitochondrial marker MitoTracker Red. **b** Average response of lyso-ExRai AMPKAR in WT (black, $n = 5$ cells from two experiments) and AMPK α KO MEFs (pink, $n = 6$ cells from two experiments) to 2-DG (40 mM) stimulation, along with maximum ratio change ($p = 9.66 \times 10^{-6}$, unpaired t -test, two-tailed). **c** Average response of mito-ExRai AMPKAR in WT (black, $n = 10$ cells from five experiments) and AMPK α KO MEFs (pink, $n = 7$ cells from three experiments) treated with 2-DG (40 mM) along with maximum ratio change ($**p = 0.0012$, unpaired t -test, two-tailed). **d** Time to half-maximal response ($t_{1/2}$) of lyso-ExRai AMPKAR (teal), cytoplasmic ExRai AMPKAR (pink), and mito-ExRai AMPKAR (black) following treatment with 2-DG ($**p = 0.0033$; $****p = 4.43 \times 10^{-10}$, one-way ANOVA with Dunnett's multiple comparisons test). **e** Average response to 2-DG (40 mM) stimulation of cytoplasmic ExRai AMPKAR in WT (black, reproduced from Fig. 1e) and LKB1 KO MEFs (pink, $n = 7$ cells from four experiments), along with maximum ratio changes ($****p = 1.57 \times 10^{-6}$, unpaired t -test, two-tailed). **f** Average response to 2-DG (40 mM) stimulation of lyso-ExRai AMPKAR in WT (black, reproduced from **b**) and LKB1 KO MEFs (pink, $n = 5$ cells from four experiments), along with maximum ratio changes ($ns p = 0.084$, unpaired t -test, two-tailed). **g** Average response to 2-DG (40 mM) stimulation of mito-ExRai AMPKAR in WT (black, reproduced from **c**) and LKB1 KO MEFs (pink, $n = 13$ cells from five experiments), along with maximum ratio changes ($ns p = 0.09$, unpaired t -test, two-tailed). **h** $t_{1/2}$ of lyso-ExRai AMPKAR (teal, $n = 6$ cells from four experiments), cytoplasmic ExRai AMPKAR (pink, $n = 5$ cells from four experiments), and mito-ExRai AMPKAR (black, $n = 10$ cells from five experiments) following treatment with 2-DG in LKB1 KO MEFs ($ns p \geq 0.55$, one-way ANOVA with Dunnett's multiple comparisons test). For all figures, time courses show the mean \pm SD, dot plots show the mean \pm SEM. Scale bars, 20 μ m.

Next, we sought to identify the mechanism underlying rapid accumulation of AMPK activity at the lysosome. Lysosomal regulation of AMPK activity is thought to occur via a multi-protein complex which coordinates the lysosomal localization of AMPK and its upstream kinase LKB1^{32,33}. We hypothesized that LKB1 plays a critical role in the fast kinetics of lysosomal AMPK activity compared to other locations. We therefore compared AMPK activity in WT and LKB1 knockout MEFs (LKB1 KO³⁷, Supplementary Fig. 2d). As a control, LKB1 KO significantly reduced 2-DG-induced cytoplasmic AMPK activity, consistent with the established prominent role of LKB1 in

mediating 2-DG-induced AMPK activity³⁸ (2-DG $\Delta R/R_0$ WT MEF 2.04 ± 0.10 ; LKB1 KO MEF 0.73 ± 0.11 , $p < 0.0001$; Fig. 2e). When we examined the 2-DG-induced lysosomal AMPK activity, we found that LKB1 KO did not affect the response amplitude of lyso-ExRai AMPKAR; strikingly the kinetics of 2-DG-induced lysosomal AMPK activity were substantially slower in LKB1 KO MEFs than in WT MEFs ($t_{1/2}$ 8.39 ± 1.14 min, $p = 0.0026$; Fig. 2f). Unexpectedly, the absence of LKB1 had minimal effect on mitochondrial AMPK activity in response to 2-DG (Fig. 2g and Supplementary Fig. 2e). The kinetics of AMPK activity at the cytoplasm, mitochondria and lysosome were similar in LKB1 KO

MEFs (Fig. 2h), indicating that LKB1 KO eliminated the kinetic advantage of lysosomal AMPK activity. These results suggest that the presence of LKB1 drives the fast kinetics of AMPK activity at the lysosome, most likely through close localization of LKB1 and AMPK at this organelle.

The lack of effect of LKB1 KO on the amplitude of lysosomal and mitochondrial AMPK activity prompted us to probe of the role of CaMKK2. 2-DG has been reported to increase intracellular calcium¹⁹, which could activate AMPK through CaMKK2. As only cytoplasmic AMPK activity was significantly diminished in the absence of LKB1, it is possible the substituting upstream kinases, such as CaMKK2, could allow for activity around membranes. To determine if CaMKK2 is involved in 2-DG-induced AMPK activity, we generated CaMKK2 KO MEFs using CRISPR/Cas9 (Supplementary Fig. 2f). We then measured AMPK activity in the cytoplasm, at the mitochondria, and lysosome (Supplementary Fig. 2g). We found that loss of CaMKK2 significantly decreased lysosomal AMPK activity ($\Delta R/R_0$ 0.42 ± 0.11 , $p = 0.0013$), suggesting CaMKK2 is important for maximal AMPK activity in response to 2-DG. In addition, loss of CaMKK2 significantly suppressed 2-DG-induced cytoplasmic and mitochondrial AMPK activity measured by ExRai AMPKAR (cytoplasm $\Delta R/R_0$ 1.06 ± 0.11 , $p < 0.0001$; mitochondria $\Delta R/R_0$ 0.17 ± 0.0041 , $p = 0.0015$). Taken together, our findings reveal spatially distinct regulatory control of LKB1 over AMPK activity in response to 2-DG, whereas loss of CaMKK2 significantly suppresses AMPK activity throughout the cell.

AMPK activity induced by allosteric activators exhibits a distinct spatial profile. Allosteric activation of AMPK, independent of energy stress or calcium signaling, is an attractive therapeutic route for treating diabetes and other metabolic disorders³⁹. Toward this goal, several synthetic ligands which bind the ADAM site have been designed^{40–42}, including MK-8722^{43,44}. Recent work has also identified endogenous ligands for the ADAM site⁴⁵. However, how ADAM site activators influence spatially compartmentalized AMPK signaling is not clear. Mechanistically, the importance of upstream kinases for ADAM site activation remains controversial^{46,47}, because ADAM site activators protect AMPK from dephosphorylation by phosphatases^{3,46,48}. As kinase and phosphatase activities can vary based on location^{12,13}, we hypothesized there could be spatially distinct differences in allosteric activator induced AMPK activity. To test this hypothesis, we set out to use ExRai AMPKAR to profile spatiotemporal AMPK activity in response to allosteric activation via the ADAM site and determine the importance of the upstream kinase LKB1 for spatially defined, allosterically activated AMPK.

We first measured MK-8722-induced cytoplasmic AMPK activity in WT and AMPK α KO MEFs, finding MK-8722 strongly induced AMPK activity in the cytoplasm (Fig. 3a). We assessed the necessity of LKB1 for MK-8722-mediated AMPK activity. In LKB1 KO MEFs, MK-8722 induced cytoplasmic AMPK activity was significantly reduced compared with WT MEFs (WT: $\Delta R/R_0 = 1.57 \pm 0.16$ vs. LKB1: $\Delta R/R_0 = 0.66 \pm 0.12$, $p < 1 \times 10^{-10}$). These data suggest that LKB1 is required for the maximal cytoplasmic AMPK activity induced by the allosteric activator MK-8722.

Next, we examined mitochondrial and lysosomal AMPK activity induced by MK-8722. WT and AMPK α KO MEFs expressing mitochondrial- or lysosomal-targeted ExRai AMPKAR were treated with MK-8722 (Fig. 3b, c). MK-8722 robustly induced AMPK activity at these locations. We found lysosomal AMPK activity was more rapid than either mitochondrial or cytoplasmic AMPK activity (4.44 ± 0.47 min, $p < 0.0001$; Fig. 3d), suggesting that there are spatially distinct differences in AMPK activity induced by allosteric activators.

LKB1 KO also showed differential effect on MK-8722 induced subcellular AMPK activities. In LKB1 KO cells expressing lysosomal-targeted ExRai AMPKAR, we found MK-8722 still induced strong lysosomal AMPK activity, but with slower kinetics compared to WT MEFs, like that observed with 2-DG treatment ($t_{1/2}$ 8.79 ± 1.68 min, $p = 0.0031$; Fig. 3c, d). On the other hand, the absence of LKB1 had minimal effect on mitochondrial AMPK activity in response to MK-8722 (Fig. 3b and Supplementary Fig. 2h), suggesting allosterically induced mitochondrial AMPK activity does not require an upstream kinase or another basally active upstream kinase is present at the mitochondria¹⁹. Together, we found the effect of ADAM site activation is not only dependent on AMPK and ADAM site ligands, but also relies on regulatory mechanisms, like upstream kinases, that are embedded in the spatiotemporal signaling network.

Nuclear AMPK activity measured using ExRai AMPKAR. AMPK has been implicated in the regulation of various nuclear targets^{8,9}, and AMPK subunits have been reported to directly localize to the nucleus⁴⁹. However, how nuclear AMPK activity is induced remains controversial^{9,10}. Biosensor-based studies have thus far been unable to conclusively shed light on the presence of nuclear activity^{16,17,50}, and some studies suggest that AMPK is active in the nucleus in response to energy stress and others failed to detect any nuclear AMPK activity^{11,51–54}. We therefore hypothesized that the enhanced sensitivity of ExRai AMPKAR would allow us to provide a more definitive view of nuclear AMPK activity.

ExRai AMPKAR was fused to a nuclear localization sequence (NLS), and we confirmed ExRai AMPKAR nuclear localization by co-localization with nuclear markers and FRAP (Fig. 4a and Supplementary Fig. 3a). In WT MEFs, we observed significant AMPK activity in the nucleus following treatment with different concentrations of 2-DG, with minimal activity detected in AMPK α KO MEFs (WT: $\Delta R/R_0 = 0.55 \pm 0.05$ vs. AMPK α KO: $\Delta R/R_0 = 0.11 \pm 0.013$, $p < 0.0001$; Fig. 4b and Supplementary Fig. 3b). Similarly, MK-8722 induced nuclear AMPK activity in WT MEFs, whereas AMPK α KO MEFs showed minimal responses from nuclear localized ExRai AMPKAR (WT: $\Delta R/R_0 = 0.43 \pm 0.030$ vs. AMPK α KO: $\Delta R/R_0 = 0.15 \pm 0.026$, $p < 0.0001$; Fig. 4c). In parallel, we directly probed for phosphorylated AMPK α in the nuclei of WT MEFs using nuclear fractionation. Cells were treated with DMSO, 2-DG, or MK-8722, and nuclear fractions collected and probed for phosphorylated AMPK α via western blotting. We found that along with cytoplasmic targets of AMPK becoming phosphorylated following treatment with 2-DG or MK-8722, nuclear pools of AMPK α were phosphorylated as well (Fig. 4d). Thus, our results provide clear evidence of nuclear AMPK activity induced by both cellular stress and allosteric activation.

Nuclear AMPK activity requires AMPK α 2 nucleo-cytoplasmic shuttling. We next investigated the mechanism behind 2-DG-induced nuclear AMPK activity. We considered two possible scenarios for nuclear AMPK activity. The first scenario considers AMPK to reside within the nucleus and become activated in situ. In the second scenario, we considered AMPK to shuttle between the cytoplasm and nucleus, with AMPK activity being initiated in the cytoplasm, followed by translocation of active AMPK into the nucleus. To differentiate between these two possibilities, we first sought to determine if AMPK translocates into the nucleus under basal and stimulated conditions. For this purpose, we focused on AMPK α 2, which has been detected in both the cytoplasm and nucleus⁴⁹. To measure AMPK translocation, we performed FRAP experiments and monitored the nuclear intensity of EGFP-tagged AMPK α 2 (EGFP-

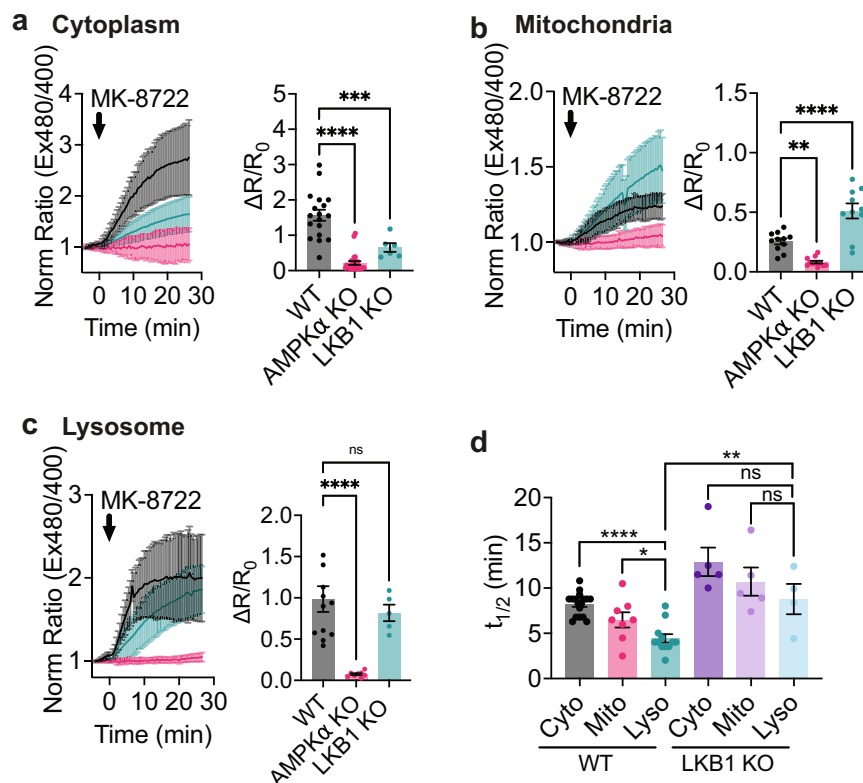


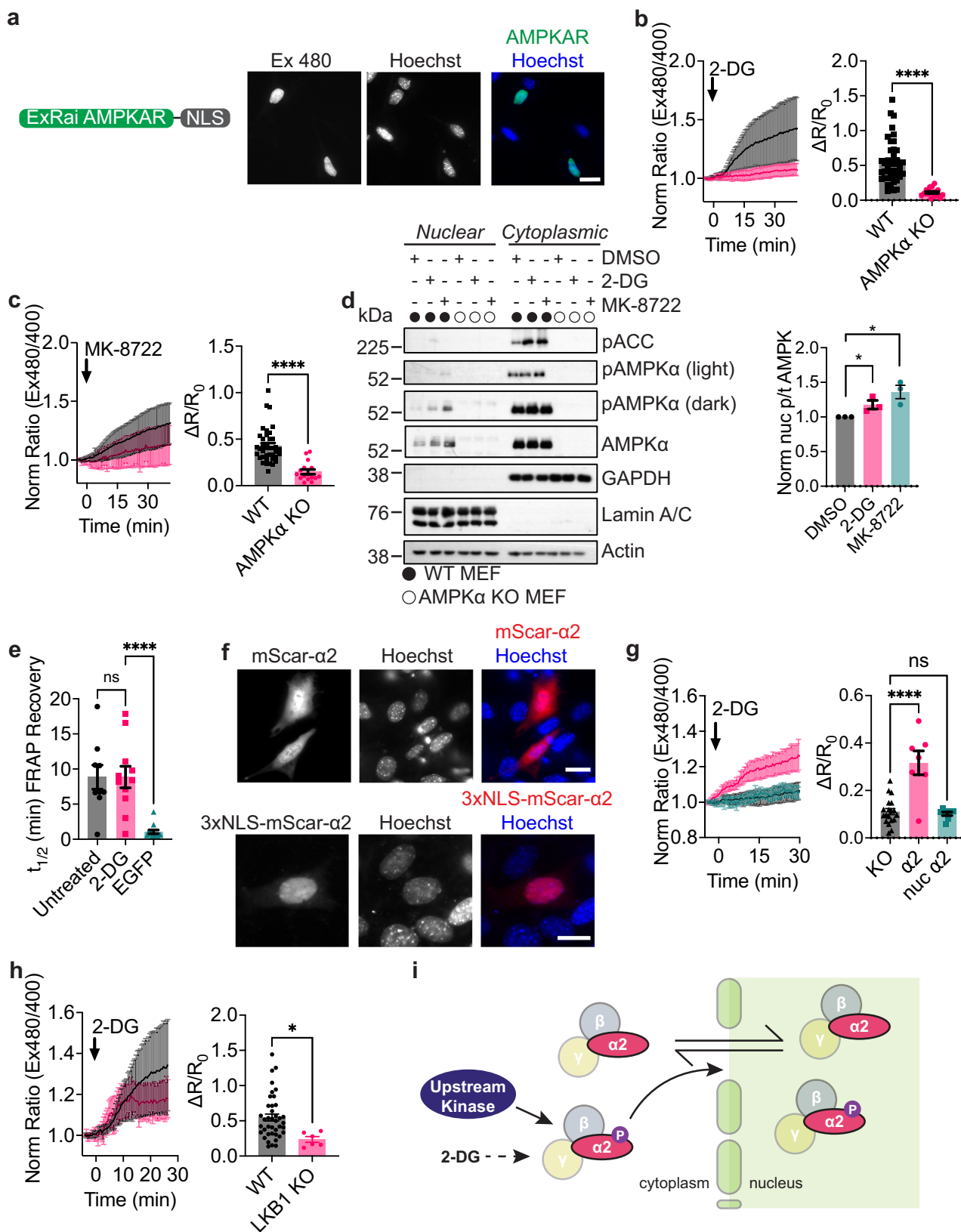
Fig. 3 AMPK activity induced by MK-8722 exhibits distinct spatiotemporal dynamics. **a** Average response of ExRai AMPKAR in WT (black, $n = 18$ cells from three experiments), AMPK α KO (pink, $n = 25$ cells from three experiments), and LKB1 KO MEFs (teal, $n = 6$ cells from four experiments) treated with MK-8722 (500 nM) along with maximum ratio change ($***p = 0.002$, $****p < 1 \times 10^{-10}$, one-way ANOVA with Dunnett's multiple comparisons test). **b** Average response of mito-ExRai AMPKAR in WT (black, $n = 11$ cells from four experiments), AMPK α KO (pink, $n = 11$ cells from three experiments), and LKB1 KO MEFs (teal, $n = 10$ cells from five experiments) treated with MK-8722 (500 nM) along with maximum ratio change ($**p = 0.0048$, $****p = 9.76 \times 10^{-5}$, one-way ANOVA with Dunnett's multiple comparisons test). **c** Average response of lyso-ExRai AMPKAR in WT (black, $n = 12$ cells from three experiments), AMPK α KO (pink, $n = 8$ cells from three experiments) and LKB1 KO MEFs (teal, $n = 5$ cells from four experiments) to MK-8722 (500 nM) stimulation, along with maximum ratio change ($ns = 0.66$, $***p < 0.0001$, one-way ANOVA with Dunnett's multiple comparisons test). **d** $t_{1/2}$ of cytoplasmic ExRai AMPKAR (black, $n = 19$ cells from three experiments), mito-ExRai AMPKAR (pink, $n = 11$ cells from four experiments), and lyso-ExRai AMPKAR (teal, $n = 12$ cells from three experiments) expressed in WT MEFs, and cytoplasmic ExRai AMPKAR (dark purple, $n = 5$ cells from four experiments), mito-ExRai AMPKAR (light purple, $n = 5$ cells from five experiments), and lyso-ExRai AMPKAR (light blue, $n = 5$ cells from four experiments) expressed in LKB1 KO MEFs following treatment with MK-8722 ($*p = 0.0203$; $****p = 1.47 \times 10^{-6}$, $ns \geq 0.18$, one-way ANOVA with Dunnett's multiple comparisons test, $**p = 0.0031$, unpaired t -test, two-tailed). For all figures, time courses show the mean \pm SD, dot plots show the mean \pm SEM.

AMPK α 2) in AMPK α KO MEFs after photobleaching of the nuclei. Under basal conditions, nuclear EGFP-AMPK α 2 intensity was fully recovered within 30 min ($t_{1/2} = 8.84 \pm 1.72$ min; Fig. 4e and Supplementary Fig. 3c). EGFP-AMPK α 2 nuclear intensity showed similar recovery kinetics following treatment with 2-DG ($t_{1/2} = 8.86 \pm 1.53$ min; $p = 0.999$). Control cells expressing EGFP alone showed full recovery of nuclear intensity within only a few minutes ($t_{1/2} = 1.06 \pm 0.26$ min, $p < 0.0001$), indicating that the slower recovery time for nuclear EGFP-AMPK α 2 fluorescence intensity is due to AMPK α 2 itself and not the EGFP tag.

We then compared the $t_{1/2}$ of EGFP-AMPK α 2 import into the nucleus to that of 2-DG-induced nuclear AMPK activity. 2-DG induced nuclear AMPK activity is slower than the half-time for EGFP-AMPK α 2 translocation into the nucleus ($t_{1/2} 15.53 \pm 1.14$ min, Supplementary Fig. 3d). This supports our second scenario; whereby activated AMPK can translocate from the cytoplasm to the nucleus to induce nuclear signaling. To test if nuclear AMPK activity is dependent on AMPK shuttling into the nucleus, we sought to localize AMPK α to the nucleus and measure nuclear AMPK activity in AMPK α KO MEFs. To sequester AMPK in the nucleus, we considered known nuclear localization and exclusion sequences

present in AMPK α ^{55,56}. However, mutating either the nuclear exclusion or localization sequence on AMPK α 2 yielded no significant effect on the nuclear localization of EGFP-tagged AMPK α 2 in HEK293T cells (Supplementary Fig. 3e). Indeed, the effects of these sequences on nuclear AMPK activity are thought to be cell-type specific. For example, the putative nuclear localization signal was identified in mouse myoblasts and found to be leptin-dependent over the course of several hours, and not functional in HEK293T cells^{55,56}. Therefore, we set out to further understand how nuclear AMPK activity is regulated by using a subcellular targeting approach.

We generated a nuclear-targeted AMPK α 2, 3xNLS-mScarlet-AMPK α 2, with untargeted mScarlet-AMPK α 2 as a control. While mScarlet-AMPK α 2 can translocate from the cytoplasm to the nucleus, the addition of three tandem NLS efficiently localizes mScarlet-AMPK α 2 to the nucleus and minimizes its exposure to the cytoplasm (Fig. 4f). We next examined the ability of these AMPK α 2 constructs to rescue nuclear AMPK activity. Untargeted mScarlet-AMPK α 2 restored nuclear AMPK activity following treatment with 2-DG in AMPK α KO MEFs ($\Delta R/R_0 = 0.39 \pm 0.063$, $p < 0.0001$; Fig. 4g), indicating that AMPK α 2 is adequate for nuclear AMPK activity. However, expression of 3xNLS-mScarlet-AMPK α 2 was



insufficient to restore nuclear AMPK activity in AMPK α KO MEFs following treatment with 2-DG ($\Delta R/R_0 = 0.10 \pm 0.0075$, $p = 0.96$). These results indicate that AMPK sequestered in the nucleus cannot respond to 2-DG stimulation and further support a mechanistic model of translocation-based nuclear AMPK activity. This suggests that nuclear AMPK activity will show a similar dependence on

upstream kinases as cytoplasmic AMPK activity. Indeed, in LKB1 KO MEFs expressing nuclear ExRai AMPKAR, we found that nuclear AMPK activity was suppressed following 2-DG treatment ($\Delta R/R_0 = 0.24 \pm 0.04$, $p = 0.021$; Fig. 4h). We validated these results in HeLa cells with and without LKB1 expression (Supplementary Fig. 3f). In CaMKK2 KO MEFs, we saw similar suppression of

Fig. 4 Nuclear AMPK activity measured using ExRai AMPKAR. **a** Domain layout and representative image of ExRai AMPKAR-NLS expressed in MEFs stained with Hoechst nuclear marker. **b** Average response of ExRai AMPKAR-NLS in either WT (black, $n = 46$ cells from five experiments) or AMPK α KO MEFs (pink, $n = 19$ cells from four experiments) treated with 2-DG (40 mM), along with maximum ratio change (**** $p = 1.51 \times 10^{-7}$, unpaired t -test, two-tailed). **c** Average response of ExRai AMPKAR-NLS in either WT (black, $n = 38$ cells from nine experiments) or AMPK α KO MEFs (pink, $n = 16$ cells from two experiments) treated with MK-8722 (500 nM), along with maximum ratio change (**** $p = 6.35 \times 10^{-7}$, unpaired t -test, two-tailed). **d** Western blot of nuclear-fractionated MEFs treated with DMSO, 2-DG (40 mM), or MK-8722 (500 nM) for 60 min. Quantification from three independent trials (* $p = 0.047$ DMSO vs. 2-DG; 0.020 DMSO vs. MK-8722, unpaired t -test, two-tailed). Full blots are shown in Source Data. **e** Half-time of FRAP recovery (min) for nuclear EGFP-AMPK $\alpha 2$ in AMPK α KO MEFs either without ($n = 9$ cells from three experiments) or with 2-DG stimulation (40 mM, $n = 11$ cells from three experiments) immediately before FRAP experiment began, or for EGFP alone ($n = 13$ cells from two experiments; ns $p = 0.999$; **** $p < 0.0001$, one-way ANOVA with Dunnett's multiple comparisons test). **f** Representative images of mScarlet-AMPK $\alpha 2$ or 3xNLS-mScarlet-AMPK $\alpha 2$ in MEFs stained with Hoechst nuclear marker. **g** Average 2-DG (40 mM)-stimulated response of AMPK α KO MEFs expressing ExRai AMPKAR-NLS alone (black, reproduced from **b**) or co-expressing mScarlet-AMPK $\alpha 2$ (pink, $n = 7$ cells from two experiments) or 3xNLS-mScarlet-AMPK $\alpha 2$ (teal, $n = 8$ cells from four experiments), along with maximum ratio change (ns $p = 0.96$; **** $p = 8.67 \times 10^{-7}$, one-way ANOVA with Dunnett's multiple comparisons test). **h** Average response of ExRai AMPKAR-NLS in either WT (black, reproduced from **b**) or LKB1 KO MEFs (pink, $n = 6$ cells from four experiments) treated with 2-DG (40 mM), along with maximum ratio change (* $p = 0.021$, unpaired t -test, two-tailed). **i** Mechanism of 2-DG-induced nuclear AMPK activity where nuclear AMPK activity in response to 2-DG is initiated in the cytoplasm dependent on upstream kinases, after which AMPK then translocates into the nucleus to phosphorylate nuclear targets. For all figures, time courses show the mean \pm SD, dot plots show the mean \pm SEM. Scale bars, 20 μ m.

nuclear AMPK activity following 2-DG treatment (Supplementary Fig. 3g). From our work, we propose a mechanistic model in which nuclear AMPK activity in response to 2-DG is initiated in the cytoplasm dependent on upstream kinases, after which AMPK then translocates into the nucleus to phosphorylate nuclear targets (Fig. 4i).

Discussion

Genetically encoded fluorescent protein-based kinase activity reporters have become essential tools to investigate compartmentalized signaling networks. In the present study, we designed and used a single-fluorophore AMPK activity reporter, ExRai AMPKAR, the most sensitive AMPK activity reporter thus far developed. While FRET-based AMPKARs have been successfully used to interrogate AMPK activity^{16–19}, the limited dynamic range of FRET-based reporters significantly limits their application. ExRai AMPKAR has over 3-times higher dynamic range, enabling detection of subtle changes in AMPK activity. This allowed us to clearly detect nuclear AMPK activity, which has posed a challenge for FRET-based AMPKARs^{16,17}. Future engineering efforts will focus on enhancing the dynamic range of some of the subcellularly targeted variants, as mito-ExRai AMPKAR exhibited a reduced dynamic range compared to an untargeted counterpart, presumably due to close proximity with membranes, as we have seen previously with other targeted biosensors^{16,57}. We found that switching the reporting unit could affect the kinetics of the response (Fig. 1f)²⁰, but the kinetics of ExRai AMPKAR correlate well with the phosphorylation of endogenous AMPK substrates (Supplementary Fig. 1c–e). Like FRET AMPKAR^{16,19}, ExRai AMPKAR could be used to assess basal AMPK activities, especially by observing the dynamic changes induced by inhibitor treatment at the resting state, a strategy which has been successfully used with FRET-based kinase activity reporters^{14,58–60}. Overall, ExRai AMPKAR represents a significant advancement in the sensitive detection of subcellular AMPK activity, and enables the robust visualization of subtle, subcellular AMPK signaling events.

Using ExRai AMPKAR, we interrogated the spatiotemporal dynamics of AMPK activity in response to two stimuli: cellular stress and allosteric activation by ADAM site ligands. We found that lysosomal AMPK activity was more rapidly induced compared to mitochondrial or cytoplasmic AMPK activity by either cellular stress or allosteric activation. As the lysosome has been suggested to function as a signaling hub^{36,39}, the rapid accumulation of AMPK activity at the lysosome could provide an advantage to substrates in proximity. Interestingly, we show that

irrespective of the mode of activation, via cellular stress or allosteric activation, the kinetic trend for spatial AMPK activity is the same, suggesting the lysosome is a privileged location for AMPK to sense and respond to a variety of different activating signals.

Building on these findings, we investigated the necessity of LKB1 for subcellular AMPK activity. At the lysosome, loss of LKB1 was associated with slower kinetics of AMPK activity, consistent with the demonstration of an AMPK regulatory complex at the lysosome consisting of AXIN, LKB1, and lysosomal membrane proteins such as vATPase and Ragulator³³. While cytoplasmic AMPK activity was significantly diminished in the absence of LKB1, we found that LKB1 is not required for maximal lysosomal or mitochondrial AMPK activity. Consistent with our findings, AMPK activity has been detected in LKB1-deficient cells stimulated with 2-DG, which was abolished upon deletion or inhibition of CaMKK2¹⁹. In our studies, we found CaMKK2 is needed for maximal AMPK activity in response to 2-DG, suggesting both LKB1 and CaMKK2 are needed for rapid and maximal AMPK activity in response to cellular stress. The necessity of upstream kinases for the effect of ADAM site activators is debated^{46,47}, and our studies show location-specific dependence of MK-8722 on LKB1 to stimulate AMPK activity. While MK-8722 did not maximally induce AMPK activity in the cytoplasm in the absence of LKB1, impacts on MK-8722-induced AMPK activity at the mitochondria and lysosome were minimal. While our studies investigate the spatiotemporal roles of upstream kinases of AMPK, spatial differences in AMPK activity could also be due to subcellular differences in phosphatase activities^{61–63}, requiring further investigation.

With the increased sensitivity of ExRai AMPKAR, we report nuclear AMPK activity in response to treatment with 2-DG and MK-8722 and propose a mechanism for 2-DG-induced nuclear AMPK activity (Fig. 4i). Basally, AMPK $\alpha 2$ can translocate between the cytoplasm and nucleus. As macromolecules larger than 40 kDa typically require the assistance of nuclear transport factors to cross the nuclear membrane⁶⁴, future studies are needed to identify the molecular determinants responsible for shuttling AMPK, which comprises three subunits with a combined molecular weight > 100 kDa⁶⁵. Our FRAP experiments suggested that the kinetics of AMPK nuclear shuttling are not affected by 2-DG. However, subcellular fractionation revealed slight increases in nuclear AMPK levels upon 2-DG stimulation (Fig. 4d). Substantial translocation and accumulation of AMPK α subunits to the nucleus were reported after long-term treatment with leptin or adiponectin⁵⁶, suggesting time- and stimulation-dependent

accumulation of nuclear AMPK. Finally, we found that nuclear AMPK activity is reliant on LKB1 and CaMKK2. Others have reported that LKB1 is primarily active in the cytoplasm^{66–68}, consistent with our model of LKB1 phosphorylating cytoplasmic AMPK, followed by nuclear translocation of phosphorylated AMPK to lead to subsequent nuclear activity. CaMKK2 is reported to be primarily localized to cytoplasm⁶⁹, further suggesting nuclear AMPK activity originates in the cytoplasm. As our model suggests constant shuttling of AMPK between the cytoplasm and nucleus, it is possible that active AMPK is shuttled back to the cytoplasm, where it could be dephosphorylated. Taken together, our results present a model of nuclear AMPK activity.

Our nuclear studies were limited to investigation of AMPK α 2-containing complexes. We focused on AMPK α 2 due to the known nuclear localization of this subunit⁴⁹. However, emerging evidence suggests that AMPK α 1 is vital for calcium-induced nuclear AMPK activity. Etoposide treatment specifically induced CaMKK2-dependent AMPK activity in the nucleus, but only with AMPK α 1-containing complexes, even in the presence of AMPK α 2 complexes⁷⁰. CaMKK2-dependent AMPK activity has also been reported in response to a variety of physiological and pharmacological agents which increase intracellular calcium^{71–76}, also dependent on AMPK α 1^{74,76–78}. In this work, we have shown that AMPK α 2 is sufficient for stress-induced nuclear AMPK activity. Input-dependent AMPK α isoform specificity could provide another level of control over nuclear AMPK activity. These additional regulatory controls would ensure precise tuning of nuclear AMPK activity and allow the kinase to discriminate between downstream effectors.

In summary, we have generated a single-fluorophore excitation-ratiometric AMPK activity reporter, which we have used to uncover mechanisms of compartmentalized AMPK activity. Using our reporter, precise and sensitive investigation into spatial AMPK signaling is now possible, which should lead to a better understanding of metabolic regulation throughout the cell.

Methods

Materials. 2-deoxyglucose (2-DG, Sigma, D6134-250MG) was dissolved in 1x DPBS. SBI-0206965 (Cayman Chemical, 18477) and MK-8722 (Aobious, AOB33226) were dissolved in DMSO (Sigma-Aldrich). Hoescht 33342 (Cell Signaling, 4082S) and puromycin (Sigma-Aldrich, P9620) were dissolved in deionized water. For western blotting and immunostaining, antibodies from Cell Signaling Technologies (Denver, MA USA) were used at 1:1000 dilution unless otherwise noted: P-ACC S79 (3661), P-AMPK T172 (2535), ACC (3662), AMPK α (2532), GAPDH (5174, 1:10,000), Laminin A/C (4777), LKB1 (3047), β -tubulin (2146, 1:10,000). From Sigma-Aldrich, anti-Actin (A5441) was diluted 1:10,000 and anti-Tubulin (T5168) was diluted 1:5000. From Santa Cruz, CaMKK2 (sc-100364) was diluted 1:500–1:1000. From Pierce, horseradish peroxidase-labeled goat anti-rabbit (PI31460) or anti-mouse (PI31430) was diluted 1:1000–1:10,000. Lipofectamine 2000 (11668019) was purchased from Thermo Fisher, and FuGENE HD (E2311) was purchased from Promega. MitoTracker Red (M22425) and LysoTracker Red (L7528) were purchased from Thermo Fisher and diluted in DMSO.

Plasmids. All primers used for molecular cloning can be found in Supplementary Table 1. To generate ExRai AMPKAR, DNA fragments encoding cpGFP and FHA1 binding domain and linker pair candidates obtained for our protein kinase A sensor ExRai AKAR²¹ were digested with SacI and EcoRI restriction enzymes (Thermo Fisher, FD1134 and FD0275, respectively) and ligated into a SacI/EcoRI-digested pRSET-B backbone containing an AMPK substrate sequence. These constructs were then subcloned into the pcDNA3 vector via digestion with BamHI (Thermo Fisher FD1464) and EcoRI restriction enzymes. ExRai AMPKAR T/A was generated via Gibson Assembly using NEBuilder HiFi DNA Assembly Kit (New England Biolabs E2621) using primers 1–2. Mitochondrial (MAIQLRSLF-PLALPGMLALLGWWFFSRKKADP), and nuclear (PKKKRQVEDA) ExRai AMPKAR were made by PCR-amplifying ExRai AMPKAR using primers 3–6 followed by insertion into BamHI/EcoRI-digested vector backbones containing the indicated localization sequences. Lysosomal ExRai AMPKAR was made by inserting PCR-amplified lysosome-associated membrane protein 1 (LAMP1) generated using primers 7–8 into HindIII (Thermo Fisher FD0504)/BamHI-digested ExRai AMPKAR backbone. mScarlet-AMPK α 2 and 3xNLS-mScarlet-AMPK α 2

(NLS targeting: PKKKRQVEDPKKKRQVEDPKKKRQVED) in pEGFP-N1 expression vector were generated via Gibson Assembly using primers 9–12. AMPK α 2 mutants were generated using primers 13–14. Generation of gRNA-containing plasmids for knockout of CaMKK2 are described below. Successful clone generation was confirmed by Sanger sequencing (Genewiz). FRET-based ABKAR¹⁸ and mCherry-LKB1¹⁸ were previously reported. EGFP-AMPK α 2⁵⁵ was a gift from Jay Brenman (Addgene plasmid 30310). H2B-mCherry was a gift from Michael Davidson (Addgene plasmid 55055). pVSVg was a gift from Bob Weinberg (Addgene plasmid 8454). psPAX2 was a gift from Didier Trono (Addgene plasmid 12260). lentiCRISPR v2 was a gift from Feng Zhang (Addgene plasmid 52961).

Cell culture and transfection. HEK293T cells were acquired from ATCC and cultured in Dulbecco's modified Eagle medium (DMEM; Gibco 11885-084) containing 1 g/l glucose, 10% fetal bovine serum (FBS, Gibco 26140-079), and 1% (v/v) penicillin-streptomycin (Pen/Strep, Gibco 15140-122). WT MEFs, AMPK KO MEFs, and LKB1 KO MEFs were described previously^{28,37} and cultured in DMEM (Gibco 11995-065) containing 4.5 g/l glucose, pyruvate, and L-glutamine, supplemented with 10% FBS and 1% Pen-Strep. CaMKK2 KO MEFs were generated as described below and were cultured in the same MEF medium. Cos7 cells were obtained from ATCC and cultured under the same conditions as MEFs. All cells were grown in humidified incubators kept at 37 °C and 5% CO₂ (HeraCell) and checked for mycoplasma using Hoechst staining. For transfection, cells were plated on 35-mm glass-bottomed dishes (CellVis D35-14-1.5-N). Cells were transfected 2–24 h after plating. HEK293T cells and Cos7 cells were transfected with DNA using Lipofectamine 2000, and MEFs were transfected with DNA using FuGENE HD. Cells were imaged 24–48 h after transfection.

Generation of CaMKK2 KO MEFs using CRISPR/Cas9. CaMKK2 knockouts were generated using the LentiCRISPR v2 strategy as previously described^{79,80}. Guide RNAs were designed using Benchling guide design tool (www.benchling.com/crispr, N- GCCAGCTTGACAACACCAT -C). Oligonucleotides from IDT were phosphorylated, annealed, and ligated into LentiCRISPR vector v2-Puro digested with BsmB1 (New England Biolabs R0739). Lentiviruses were produced by co-transfection of the lentiviral backbone constructs and packaging plasmids pVSVg and psPAX2 in 293T cells. Lipofectamine 2000 was used as a transfection reagent at a ratio of 3:1 lipofectamine/DNA. Lentivirus was collected 72 h after transfection. MEFs were infected with 0.45 μ M-filtered lentiviral supernatant supplemented with polybrene (Sigma-Aldrich 107689) for 24 h. Cells recovered for 24 h and then were selected with 2.5 μ M/ml puromycin. Polyclonal pools were screened for target deletion by western blot. The pools confirmed to stably express sgRNAs were single-cell sorted into 96 well plates. Monoclonal lines were expanded from single cells and their knockout status was then determined by western blot to use for subsequent experiments.

Fluorescence imaging and image analysis. For all live cell imaging experiments, cells were washed and incubated in Hanks balanced salt solution (HBSS, Gibco 14065-056; buffered with 20 mM HEPES, pH 7.4 and supplemented with 2 g/l glucose) for at least 30 min at 37 °C prior to imaging. All imaging was performed in the dark at 37 °C. 2-DG (40 mM), MK-8722 (500 nM), and SBI-0206965 (30 μ M) were added at the indicated times.

Time-lapse epifluorescence images were acquired on either a Zeiss AxioObserver Z1 microscope (Carl Zeiss) equipped with a plan-apochromat \times 20/0.8 N/A and \times 40/1.4 N/A objectives (Carl Zeiss) and CMOS Orca Flash 4.0 camera (Hamamatsu) enclosed in a custom incubator, or a Zeiss AxioObserver Z7 microscope equipped with a \times 40/1.4 N/A objective, Prime 95B sCMOS camera (Photometrics), and stage-top incubator (Carl Zeiss). Imaging experiments were done using a modified version of the open-source MATLAB (Mathworks) and μ manager (Micro-Manager)-based MATScope imaging suite (GitHub, see Code Availability statement). Dual GFP excitation-ratio imaging was accomplished using ET405/40x and ET480/30x excitation filters with a T505dxc dichroic, and a ET535/50 m emission filter. EGFP was imaged using an ET480/30x excitation filter with a T505dxc dichroic, and ET535/50 m emission filter. mCherry and mScarlet were imaged using an HQ568/55x excitation filter with a Q600LPx dichroic and HQ653/95 m emission filter. Dual cyan/yellow emission ratio imaging was performed using an ET420/20x excitation filter, a T4551pct dichroic, and two emission filters (ET470/40 m for CFP and ET535/25 m for YFP). CFP imaging was done using ET420/20x excitation filter with a T4551pct dichroic and AT470/40 m emission filter. YFP imaging was done using ET495/10x excitation filter with a T5151p dichroic and ET535/25 m emission filter. All filter sets were controlled by an external filter-exchanger (Prior Scientific or Ludl Electronic Products, Ltd). Exposure times ranged between 50 to 100 ms, and images were acquired every 15–60 s.

Image analysis for time-lapse imaging was done using custom MATLAB code. Regions of interest (ROI) were randomly selected in cells throughout the field of view. For localized biosensors, ROIs were selected around the mitochondria, a region of the cell containing lysosomes, or the entire nucleus. Raw fluorescence intensities were corrected for background fluorescence using a cell-free area. cpGFP excitation ratios (Ex480/400) and yellow/cyan FRET emission ratios were calculated for each time point. Ratios were normalized to values before drug

stimulation. Maximum ratio changes ($\Delta R/R_0$) were calculated as $(R_{\max} - R_0)/R_0$, where R is the excitation or emission ratio. SNR for each cell was calculated by dividing the maximum ratio change by the standard deviation of the baseline before drug addition. Z-factors were calculated as $1 - (3\sigma_{\max \text{ response average}} + 3\sigma_{\text{baseline average}})/|\sigma_{\max \text{ response average}} - \sigma_{\text{baseline average}}|$. Further data analysis was done using Microsoft Excel Version 16. Graphs were plotted using GraphPad Prism 8 and 9 (GraphPad Software).

FRAP experiments were performed on a Nikon Ti2 C2 confocal microscope equipped with a 40×1.3 NA oil objective (Nikon), 405 nm, 488 nm, and 561 nm laser lines, C2-DUVB GaAsP detector, and Okolabs stage-top incubator. The microscope was controlled using NIS-Elements software (High content analysis package, Nikon). Nuclei were identified by H2B-mCherry expression. The entire nucleus was selected for photobleaching, or for biosensor, region of the cell expressing the biosensor. The ROI was photobleached for 1 s with 100% 488 nm laser power or 2 s with 100% 488 nm and 25% 405 nm laser power and observed for 3–25 min post-bleaching. Unnormalized intensity data was collected using NIS-Elements and normalized using Excel (Microsoft). FRAP curves were fit to a single exponential recovery equation using the curve fitting tool in FIJI [ImageJ] (FIJI)⁸¹, $y = a(1 - e^{-bx}) + c$.

Pseudocolor images were created using FIJI.

Western blotting. MEFs were plated in either 6- or 10-cm dishes in growth medium. Cells were treated with small molecules and scraped on ice and pelleted in PBS. PBS was aspirated and the cells were lysed in lysis buffer (3× radio-immunoprecipitation assay buffer, protease inhibitor cocktail (Roche 1169749801), 1 mM phenylmethylsulfonyl fluoride, 1 mM sodium pervanadate, 1 mM sodium fluoride, and 25 mM calyculin A). Protein samples were separated using 4–15% SDS-PAGE (BioRad 456-1085) and transferred to nitrocellulose membranes. Membranes were blocked using 1% bovine serum albumin (Sigma-Aldrich 03116956001 in 1× TBS, 0.05% Tween-20) and incubated with primary antibodies overnight at 4 °C. After incubation with the appropriate horseradish peroxidase-conjugated secondary antibody, bands were visualized by chemiluminescence. Uncropped full blots are available in the Source Data.

Nuclear fractionation. MEFs were seeded at a density of 6×10^6 cells per 15-cm dish in growth medium 18 h prior to treatment. Small molecules were applied to cells and incubated for 60 min at 37 °C: DMSO (3 μl/ml), 2-DG (40 mM), MK-8722 (500 nM). Cells were scraped on ice and pelleted in PBS. PBS was aspirated and cells were taken forward for nuclear/cytoplasmic fractionation using NE-PER kit (Thermo Fisher Scientific, 78835) following manufacturer's protocol, or for whole-cell lysate control samples. Fractionation was performed using WT MEFs and AMPK KO MEFs. Parallel whole-cell lysates were generated using CST lysis buffer (20 mM Tris, pH 7.5, 150 mM NaCl, 1 mM EDTA, 1 mM EGTA, 1% Triton X-100, 2.5 mM pyrophosphate, 50 mM NaF, 5 mM β-glycero-phosphate, 50 nM calyculin A, 1 mM Na₂VO₄, and protease inhibitors). Lysates were incubated at 4 °C for 15 min and cleared at 16,000 × g for 10 min at 4 °C. Total protein was normalized using the BCA Protein Assay kit (Pierce 23225).

Statistics and reproducibility. Figure preparation and statistical analysis were performed using GraphPad Prism 8 or 9. For comparison of two parametric data sets, Student's *t* test was used. Nonparametric tests were done using Mann–Whitney *U*. For comparing three or more sets of data, ordinary one-way ANOVA followed by multiple comparisons test was done. Statistical significance was defined as $p < 0.05$ with a 95% confidence interval. The number of cells analyzed (*n* cell) and number of independent experiments are reported in all figure legends. All time courses shown are the mean of all cells ± standard deviation unless otherwise noted. All dot plots shown depict the mean ± standard error of the mean.

Reporting summary. Further information on research design is available in the Nature Research Reporting Summary linked to this article.

Data availability

The plasmids utilized in this article will be submitted to the non-profit plasmid repository, Addgene, for scientific sharing. Source data are provided with this paper.

Code availability

Custom MATLAB code used for image acquisition and analysis is available at <https://github.com/jinzhanglab-ucsd/MatScopeSuite> (<https://doi.org/10.5281/zenodo.5908008>).

Received: 19 October 2021; Accepted: 6 June 2022;

Published online: 05 July 2022

References

- Herzig, S. & Shaw, R. J. AMPK: guardian of metabolism and mitochondrial homeostasis. *Nat. Rev. Mol. Cell Biol.* **19**, 121–135 (2018).
- Xiao, B. et al. Structure of mammalian AMPK and its regulation by ADP. *Nature* **472**, 230–233 (2011).
- Xiao, B. et al. Structural basis of AMPK regulation by small molecule activators. *Nat. Commun.* **4**, 3017 (2013).
- Woods, A. et al. LKB1 is the upstream kinase in the AMP-activated protein kinase cascade. *Curr. Biol.* **13**, 2004–2008 (2003).
- Shaw, R. J. et al. The tumor suppressor LKB1 kinase directly activates AMP-activated kinase and regulates apoptosis in response to energy stress. *Proc. Natl Acad. Sci. USA* **101**, 3329–3335 (2004).
- Woods, A. et al. Ca²⁺/calmodulin-dependent protein kinase kinase-β acts upstream of AMP-activated protein kinase in mammalian cells. *Cell Metab.* **2**, 21–33 (2005).
- Garcia, D. & Shaw, R. J. AMPK: mechanisms of cellular energy sensing and restoration of metabolic balance. *Mol. Cell* **66**, 789–800 (2017).
- Hardie, D. G., Schaffer, B. E. & Brunet, A. AMPK: an energy-sensing pathway with multiple inputs and outputs. *Trends Cell Biol.* **26**, 190–201 (2016).
- Khan, A. S. & Frigo, D. E. A spatiotemporal hypothesis for the regulation, role, and targeting of AMPK in prostate cancer. *Nat. Rev. Urol.* **14**, 164–180 (2017).
- Chauhan, A. S., Zhuang, L. & Gan, B. Spatial control of AMPK signaling at subcellular compartments. *Crit. Rev. Biochem. Mol. Biol.* **55**, 17–32 (2020).
- Zong, Y. et al. Hierarchical activation of compartmentalized pools of AMPK depends on severity of nutrient or energy stress. *Cell Res.* **29**, 1–14 (2019).
- Mehta, S. & Zhang, J. Illuminating the cell's biochemical activity architecture. *Biochemistry* **56**, 5210–5213 (2017).
- Mehta, S. & Zhang, J. Biochemical activity architectures visualized—using genetically encoded fluorescent biosensors to map the spatial boundaries of signaling compartments. *Acc. Chem. Res.* **54**, 2409–2420 (2021).
- Zhou, X. et al. Dynamic visualization of mTORC1 activity in living cells. *Cell Rep.* **10**, 1767–1777 (2015).
- Depry, C., Mehta, S., Li, R. & Zhang, J. Visualization of compartmentalized kinase activity dynamics using adaptable BimKARs. *Chem. Biol.* **22**, 1470–1479 (2015).
- Miyamoto, T. et al. Compartmentalized AMPK signaling illuminated by genetically encoded molecular sensors and actuators. *Cell Rep.* **11**, 657–670 (2015).
- Tsou, P., Zheng, B., Hsu, C. H., Sasaki, A. T. & Cantley, L. C. A fluorescent reporter of AMPK activity and cellular energy stress. *Cell Metab.* **13**, 476–486 (2011).
- Sample, V., Ramamurthy, S., Gorshkov, K., Ronnett, G. V. & Zhang, J. Polarized activities of AMPK and BRSK in primary hippocampal neurons. *Mol. Biol. Cell* **26**, 1935–1946 (2015).
- Konagaya, Y. et al. A highly sensitive FRET biosensor for AMPK exhibits heterogeneous AMPK responses among cells and organs. *Cell Rep.* **21**, 2628–2638 (2017).
- Mehta, S. et al. Single-fluorophore biosensors for sensitive and multiplexed detection of signalling activities. *Nat. Cell Biol.* **20**, 1215–1225 (2018).
- Zhang, J. et al. An ultrasensitive biosensor for high-resolution kinase activity imaging in awake mice. *Nat. Chem. Biol.* **118**, 11707–11724 (2020).
- Greenwald, E. C., Mehta, S. & Zhang, J. Genetically encoded fluorescent biosensors illuminate the spatiotemporal regulation of signaling networks. *Chem. Rev.* **118**, 11707–11794 (2018).
- Schmitt, D. L., Mehta, S. & Zhang, J. Illuminating the kinome: visualizing real-time kinase activity in biological systems using genetically encoded fluorescent protein-based biosensors. *Curr. Opin. Chem. Biol.* **54**, 63–69 (2020).
- Nasu, Y., Shen, Y., Kramer, L. & Campbell, R. E. Structure- and mechanism-guided design of single fluorescent protein-based biosensors. *Nat. Chem. Biol.* **17**, 509–518 (2021).
- Lobas, M. A. et al. A genetically encoded single-wavelength sensor for imaging cytosolic and cell surface ATP. *Nat. Commun.* **10**, 1–13 (2019).
- Dite, T. A. et al. AMP-activated protein kinase selectively inhibited by the type II inhibitor SBI-0206965. *J. Biol. Chem.* **293**, 8874–8885 (2018).
- Ahwazi, D. et al. Investigation of the specificity and mechanism of action of the ULK1/AMPK inhibitor SBI-0206965. *Biochem J.* **478**, 2977–2997 (2021).
- Toyama, E. Q. et al. AMP-activated protein kinase mediates mitochondrial fission in response to energy stress. *Science* **351**, 275–281 (2016).
- Kosaisawe, N., Sparta, B., Pargett, M., Teragawa, C. K. & Albeck, J. G. Transient phases of OXPHOS inhibitor resistance reveal underlying metabolic heterogeneity in single cells. *Cell Metab.* **33**, 649–665.e8 (2021).
- Zhang, J., Chung, T. & Oldenburg, K. A simple statistical parameter for use in evaluation and validation of high throughput screening assays. *J. Biomol. Screen.* **4**, 67–73 (1999).
- Egan, D. F. et al. Phosphorylation of ULK1 (hATG1) by AMP-activated protein kinase connects energy sensing to mitophagy. *Science* **331**, 456–461 (2011).
- Zhang, Y.-L. et al. AMP as a low-energy charge signal autonomously initiates assembly of AXIN-AMPK-LKB1 complex for AMPK activation. *Cell Metab.* **18**, 546–555 (2013).

33. Zhang, C.-S. et al. The lysosomal v-ATPase-Ragulator complex is a common activator for AMPK and mTORC1, acting as a switch between catabolism and anabolism. *Cell Metab.* **20**, 526–540 (2014).
34. Zhang, C.-S. et al. Fructose-1,6-bisphosphate and aldolase mediate glucose sensing by AMPK. *Nature* **548**, 112–116 (2017).
35. Li, M. et al. Aldolase is a sensor for both low and high glucose, linking to AMPK and mTORC1. *Cell Res.* **31**, 1–4 (2020).
36. Lin, S.-C. & Hardie, D. G. AMPK: sensing glucose as well as cellular energy status. *Cell Metab.* **27**, 299–313 (2018).
37. Goodwin, J. M. et al. An AMPK-independent signaling pathway downstream of the LKB1 tumor suppressor controls Snail1 and metastatic potential. *Mol. Cell* **55**, 436–450 (2014).
38. Corradetti, M. N., Inoki, K., Bardeesy, N., DePinho, R. A. & Guan, K. L. Regulation of the TSC pathway by LKB1: evidence of a molecular link between tuberous sclerosis complex and Peutz-Jeghers syndrome. *Gene Dev.* **18**, 1533–1538 (2004).
39. Trefz, E. & Shaw, R. J. AMPK: restoring metabolic homeostasis over space and time. *Mol. Cell* **81**, 3677–3690 (2021).
40. Cameron, K. O. et al. Discovery and preclinical characterization of 6-chloro-5-[4-(1-hydroxycyclobutyl)phenyl]-1 H-indole-3-carboxylic acid (PF-06409577), a direct activator of adenosine monophosphate-activated protein kinase (AMPK), for the potential treatment of diabetic nephropathy. *J. Med. Chem.* **59**, 8068–8081 (2016).
41. Cokorinos, E. C. et al. Activation of skeletal muscle AMPK promotes glucose disposal and glucose lowering in non-human primates and mice. *Cell Metab.* **25**, 1147–1159.e10 (2017).
42. Steneberg, P. et al. PAN-AMPK activator O304 improves glucose homeostasis and microvascular perfusion in mice and type 2 diabetes patients. *JCI Insight* **3**, e99114 (2018).
43. Feng, D. et al. Discovery of MK-8722: a systemic, direct pan-activator of AMP-activated protein kinase. *ACS Med. Chem. Lett.* **9**, 39–44 (2017).
44. Myers, R. W. et al. Systemic pan-AMPK activator MK-8722 improves glucose homeostasis but induces cardiac hypertrophy. *Science* **357**, 507–511 (2017).
45. Pinkosky, S. L. et al. Long-chain fatty acyl-CoA esters regulate metabolism via allosteric control of AMPK β 1 isoforms. *Nat. Metab.* **2**, 873–881 (2020).
46. Göransson, O. et al. Mechanism of action of A-769662, a valuable tool for activation of AMP-activated protein kinase. *J. Biol. Chem.* **282**, 32549–32560 (2007).
47. Willows, R. et al. Phosphorylation of AMPK by upstream kinases is required for activity in mammalian cells. *Biochem J.* **474**, 3059–3073 (2017).
48. Sanders, M. J. et al. Defining the mechanism of activation of AMP-activated protein kinase by the small molecule A-769662, a member of the thienopyridone family. *J. Biol. Chem.* **282**, 32539–32548 (2007).
49. Salt, I. et al. AMP-activated protein kinase: greater AMP dependence, and preferential nuclear localization, of complexes containing the α 2 isoform. *Biochem J.* **334**, 177–187 (1998).
50. Pelosse, M. et al. Synthetic energy sensor AMPfret deciphers adenylate-dependent AMPK activation mechanism. *Nat. Commun.* **10**, 1038 (2019).
51. Greer, E. L. et al. The energy sensor AMP-activated protein kinase directly regulates the mammalian FOXO3 transcription factor. *J. Biol. Chem.* **282**, 30107–30119 (2007).
52. Kodiha, M., Rassi, J. G., Brown, C. M. & Stochaj, U. Localization of AMP kinase is regulated by stress, cell density, and signaling through the MEK→ERK1/2 pathway. *Am. J. Physiol. Cell Physiol.* **293**, C1427–C1436 (2007).
53. Kodiha, M., Ho-Wo-Cheong, D. & Stochaj, U. Pharmacological AMP-kinase activators have compartment-specific effects on cell physiology. *Am. J. Physiol. Cell Physiol.* **301**, C1307–C1315 (2011).
54. Shin, H.-J. R. et al. AMPK-SKP2–CARM1 signalling cascade in transcriptional regulation of autophagy. *Nature* **534**, 553–557 (2016).
55. Kazgan, N., Williams, T., Forsberg, L. J. & Brenman, J. E. Identification of a nuclear export signal in the catalytic subunit of AMP-activated protein kinase. *Mol. Biol. Cell* **21**, 3433–3442 (2010).
56. Suzuki, A. et al. Leptin stimulates fatty acid oxidation and peroxisome proliferator-activated receptor α gene expression in mouse C2C12 myoblasts by changing the subcellular localization of the α 2 form of AMP-activated protein kinase. *Mol. Cell Biol.* **27**, 4317–4327 (2007).
57. Chen, M., Sun, T., Zhong, Y., Zhou, X. & Zhang, J. A highly sensitive fluorescent Akt biosensor reveals lysosome-selective regulation of lipid second messengers and kinase activity. *ACS Cent. Sci.* **7**, 2009–2020 (2021).
58. Gallegos, L. L., Kunkel, M. T. & Newton, A. C. Targeting protein kinase C activity reporter to discrete intracellular regions reveals spatiotemporal differences in agonist-dependent signaling. *J. Biol. Chem.* **281**, 30947–30956 (2006).
59. Kajimoto, T., Sawamura, S., Tohyama, Y., Mori, Y. & Newton, A. C. Protein kinase C δ -specific activity reporter reveals agonist-evoked nuclear activity controlled by Src family of kinases. *J. Biol. Chem.* **285**, 41896–41910 (2010).
60. Fosbrink, M., Aye-Han, N.-N., Cheong, R., Levchenko, A. & Zhang, J. Visualization of JNK activity dynamics with a genetically encoded fluorescent biosensor. *Proc. Natl Acad. Sci. USA* **107**, 5459–5464 (2010).
61. Joseph, B. K. et al. Inhibition of AMP kinase by the protein phosphatase 2A heterotrimer, PP2A Ppp2r2d. *J. Biol. Chem.* **290**, 10588–10598 (2015).
62. Taleski, G. & Sontag, E. Protein phosphatase 2A and tau: an orchestrated 'pas de deux'. *FEBS Lett.* **592**, 1079–1095 (2018).
63. Tsvetanova, N. G. et al. Endosomal cAMP production broadly impacts the cellular phosphoproteome. *J. Biol. Chem.* **297**, 100907 (2021).
64. Lin, D. H. & Hoelz, A. The structure of the nuclear pore complex (an update). *Annu. Rev. Biochem.* **88**, 1–59 (2019).
65. Cheung, P. C. F., Salt, I. P., Davies, S. P., Hardie, D. G. & Carling, D. Characterization of AMP-activated protein kinase γ -subunit isoforms and their role in AMP binding. *Biochem. J.* **346**, 659–669 (2000).
66. Lan, F., Cacicado, J. M., Ruderman, N. & Ido, Y. SIRT1 modulation of the acetylation status, cytosolic localization, and activity of LKB1. Possible role in AMP-activated protein kinase activation. *J. Biol. Chem.* **283**, 27628–27635 (2008).
67. Dorfman, J. & Macara, I. G. STRAD α regulates LKB1 localization by blocking access to importin- α , and by association with Crm1 and exportin-7. *Mol. Biol. Cell* **19**, 1614–1626 (2008).
68. Xie, Z. et al. Identification of the serine 307 of LKB1 as a novel phosphorylation site essential for its nucleocytoplasmic transport and endothelial cell angiogenesis. *Mol. Cell Biol.* **29**, 3582–3596 (2009).
69. Thul, P. J. et al. A subcellular map of the human proteome. *Science* **356**, eaal3321-14 (2017).
70. Vara-Ciruelos, D. et al. Genotoxic damage activates the AMPK- α 1 isoform in the nucleus via Ca²⁺/CaMKK2 signaling to enhance tumor cell survival. *Mol. Cancer Res.* **16**, 345–357 (2018).
71. Li, S. et al. Ca²⁺-stimulated AMPK-dependent phosphorylation of Exo1 protects stressed replication forks from aberrant resection. *Mol. Cell* **74**, 1123–1137.e6 (2019).
72. Stahmann, N., Woods, A., Carling, D. & Heller, R. Thrombin activates AMP-activated protein kinase in endothelial cells via a pathway involving Ca²⁺/calmodulin-dependent protein kinase kinase β . *Mol. Cell Biol.* **26**, 5933–5945 (2006).
73. Thornton, C., Sardini, A. & Carling, D. Muscarinic receptor activation of AMP-activated protein kinase inhibits orexinergic neuropeptide mRNA expression. *J. Biol. Chem.* **283**, 17116–17122 (2008).
74. Tamás, P. et al. Regulation of the energy sensor AMP-activated protein kinase by antigen receptor and Ca²⁺ in T lymphocytes. *J. Exp. Med.* **203**, 1665–1670 (2006).
75. Hawley, S. A. et al. Calmodulin-dependent protein kinase kinase- β is an alternative upstream kinase for AMP-activated protein kinase. *Cell Metab.* **2**, 9–19 (2005).
76. Hurley, R. L. et al. Regulation of AMP-activated protein kinase by multisite phosphorylation in response to agents that elevate cellular cAMP. *J. Biol. Chem.* **281**, 36662–36672 (2006).
77. González, A., Hall, M. N., Lin, S.-C. & Hardie, D. G. AMPK and TOR: the yin and yang of cellular nutrient sensing and growth control. *Cell Metab.* **31**, 472–492 (2020).
78. Russell, F. M. & Hardie, D. G. AMP-activated protein kinase: do we need activators or inhibitors to treat or prevent cancer? *Int J. Mol. Sci.* **22**, 186 (2020).
79. Shalem, O. et al. Genome-scale CRISPR-Cas9 knockout screening in human cells. *Science* **343**, 84–87 (2014).
80. Sanjana, N. E., Shalem, O. & Zhang, F. Improved vectors and genome-wide libraries for CRISPR screening. *Nat. Methods* **11**, 783–784 (2014).
81. Schindelin, J. et al. Fiji: an open-source platform for biological-image analysis. *Nat. Methods* **9**, 676–682 (2012).

Acknowledgements

We thank the following: Brian Tenner, Megan Mizinski, and Daniel Nguyen for assistance with molecular cloning; Qiang Ni for support in material acquisition; Eric Greenwald for assisting with MATLAB code development; Eric Griffis and Daphne Bindels with the UC San Diego Nikon Imaging Center; and Xin Zhou, Yanghao Zhong, Allen Leung, and Padmini Rangamani for helpful discussion and critique. This work was supported by the National Institutes of Health (NIH/NCI T32 CA009523 and NIH/NIGMS K12 GM068524 to D.L.S.; R35 CA197622, R01 HL162302 and R01 DE030497 to J.Z.; and R35 CA220538 and P01 CA120964 to R.J.S.); the University of California President's Postdoctoral Fellowship (to D.L.S.); and the Air Force Office of Scientific Research (FA9500-18-1-0051 to J.Z.).

Author contributions

D.L.S. and J.Z. conceived the project; D.L.S., S.D.C., S.M., R.J.S., and J.Z. designed experiments; D.L.S., J.F.Z., M.C., S.D.C., C.Y.H., and A.C.L. performed experiments and analyzed data. J.Z. and R.J.S. coordinated the study and provided guidance. D.L.S., S.M., and J.Z. wrote the paper. All authors discussed the results and approved the final version of the manuscript.

Competing interests

The authors declare no competing interests.

Additional information

Supplementary information The online version contains supplementary material available at <https://doi.org/10.1038/s41467-022-31190-x>.

Correspondence and requests for materials should be addressed to Jin Zhang.

Peer review information *Nature Communications* thanks Michiyuki Matsuda and the other, anonymous, reviewer(s) for their contribution to the peer review of this work.

Reprints and permission information is available at <http://www.nature.com/reprints>

Publisher's note Springer Nature remains neutral with regard to jurisdictional claims in published maps and institutional affiliations.



Open Access This article is licensed under a Creative Commons Attribution 4.0 International License, which permits use, sharing, adaptation, distribution and reproduction in any medium or format, as long as you give appropriate credit to the original author(s) and the source, provide a link to the Creative Commons license, and indicate if changes were made. The images or other third party material in this article are included in the article's Creative Commons license, unless indicated otherwise in a credit line to the material. If material is not included in the article's Creative Commons license and your intended use is not permitted by statutory regulation or exceeds the permitted use, you will need to obtain permission directly from the copyright holder. To view a copy of this license, visit <http://creativecommons.org/licenses/by/4.0/>.

© The Author(s) 2022